Design Methodology of Three-Phase *LLC* Charger Based on Time-Domain Model With Enhanced Analytical Accuracy and Power Efficiency

Ning Guo, *Graduate Student Member, IEEE*, Jinjun Liu, *Fellow, IEEE*, Sixing Du, *Member, IEEE*, Cong Li, *Student Member, IEEE*, Hui Chen, *Student Member, IEEE*, and Zhifeng Deng, *Graduate Student Member, IEEE*

***Abstract*—Three-phase *LLC* converters show considerable potential in battery chargers. However, the existing parameter design methods for three-phase *LLC* converters have limitation in analytical accuracy and efficiency optimization over the wide voltage range. To address the above issues, this article proposes a time-domain model (TDM) based design method for three-phase *LLC* chargers. First, a comprehensive TDM for the three-phase *LLC* converter is developed, providing a detailed analysis of operating modes and mode distributions across the entire operating range. Then, based on TDM, a novel design method is proposed to optimize the efficiency of the entire charging process. The resonant root-mean-square current is selected as the optimization objective, and its relationship with design parameters is researched to derive the optimal constraints. Meanwhile, suitable operating modes are identified for each charging pattern to satisfy the soft-switching condition. A step-by-step design procedure is finally provided to determine the optimal parameters. The analysis proves that the proposed design methodology enhances accuracy and efficiency across the entire operating range of the three-phase *LLC* charger. The effectiveness is also validated through a 4.5-kW experimental setup with 98.1% peak efficiency.**

***Index Terms*—Charging trajectory, optimal root-mean-square (rms) current design, three-phase *LLC* converter, time-domain model (TDM).**

I. Introduction

With the rapid development of electric vehicles (EVs), the performance of EV battery chargers is becoming increasingly important. Typically, isolated dc–dc converters are employed to regulate the output voltage and current of EV chargers, hence determining the characteristics of the chargers [1]. *LLC* converters are promising candidates due to their wide soft-switching range, high efficiency, and high reliability [2], [3], [4], [5], [6]. Single-phase *LLC* converters are widely applied to low and medium power charging, while three-phase *LLC* converters are gaining more attention when pursuing higher charging speed. Compared with single-phase *LLC* converters, three-phase *LLC* converters can provide higher efficiency in high power applications, lower output current ripple, and smaller filter volume [7], [8], [9], [10], [11].

Nowadays, three-phase *LLC* chargers are facing challenging requirements: First, fulfilling the wide output voltage and power range within a given frequency range; second, maintaining high efficiency across the entire charging process [12]. Therefore, the parameters of the resonant tank should be sophisticatedly designed to ensure that the output characteristics meet these requirements. The premise of a design method is to create the accurate model to describe the characteristics of the converter. Since pulse frequency modulation (PFM) is the most frequently employed modulation strategy, researches mainly focus on the design methods under PFM. The existing parameter design methods of the three-phase *LLC* converters under PFM can be classified into two main categories based on different modeling methods: fundamental harmonic approximation (FHA) based design methods and time-domain model (TDM)-based design methods.

FHA-based methods are characterized by their simplicity and intuitiveness. The essence of FHA is applying the Fourier decomposition to the resonant tank voltage and taking only the fundamental harmonic for approximate analysis. The accuracy of FHA is high when the switching frequency is close to the resonant frequency, as the resonant waveforms approximate the sinusoidal waveforms. There are plenty of researches on FHA-based design methods for single-phase *LLC* converters [13], [14], [15]. The FHA modeling for a three-phase *LLC* converter is similar to that of a single-phase *LLC* converter. Several FHA-based design methods have been proposed for three-phase *LLC* converters. Arshadi et al. [7] design an acceptable set of parameters by iterative adjustments to fulfill the worst-case condition of the battery charger. In [16], parameters are designed by considering the constrains of voltage gain, switching frequency range, and voltage limitation of resonant capacitor. In [17], three sets of parameters are selected based

Received 3 July 2024; revised 8 November 2024; accepted 31 December 2024. Date of publication 6 January 2025; date of current version 26 February 2025. This work was supported by the National Natural Science Foundation of China under Grant 51907156. Recommended for publication by Associate Editor O. Trescases. *(Corresponding authors: Jinjun Liu; Sixing Du.)*

The authors are with the State Key Laboratory of Electrical Insulation and Power Equipment, School of Electrical Engineering, Xi'an Jiaotong University, Xi'an 710049, China (e-mail: gnlbj657@stu.xjtu.edu.cn; jjliu@mail.xjtu.edu.cn; dusixing.2011@xjtu.edu.cn; lc2000@stu.xjtu.edu.cn; chenhui_xjtu@stu.xjtu.edu.cn; happiness980102@stu.xjtu.edu.cn).

Color versions of one or more figures in this article are available at https://doi.org/10.1109/TPEL.2025.3526323.

Digital Object Identifier 10.1109/TPEL.2025.3526323

on the resonant tank analysis, and the best set is identified considering the switching frequency and magnetic components. However, all the FHA-based design methods for the three-phase *LLC* converters have common drawbacks when applied to EV chargers. The accuracy of FHA gets worse when the switching frequency deviates from the resonant frequency, as higher order harmonics are neglected due to the model's approximation. The peak voltage gains predicted by the FHA model are lower than the practical results, leading to a smaller designed magnetizing inductance and underutilization of the resonant tank. Therefore, the three-phase *LLC* charger will have higher current, reducing the efficiency.

In order to improve the analytical accuracy and realize an optimal design, the TDM-based design methods are researched. TDM constructs the state equations of the converter in segments based on the different conduction states. By solving these state equations in time domain, the characteristics of three-phase *LLC* converters can be accurately described across the entire operating range. In recent years, numerous design methods have been proposed to enhance the efficiency of single-phase *LLC* converters, leveraging the TDMs high accuracy across various operating ranges. Efficiency is a typical optimization objective when designing the converter. In [18] and [19], the efficiency at a certain load condition is optimized to determine the solution. Similarly, Wei et al. [20] focus on efficiency under the worst-case condition and locates the optimal parameters by exhaustive search. To achieve improved performance across the entire operating range, some researches adopt the weighted average efficiency. The research in [21] combines the efficiencies across varying output voltages and power to calculate weighted average efficiency. In [22] and [23], a time-weighted average efficiency is introduced for battery charger design, accounting for total conversion energy over the charging process. While taking efficiency as the optimization objective is intuitive, it is challenging to calculate losses accurately, particularly for magnetic components. The calculation of efficiency could be complicated, as some specific devices should be selected in advance. Therefore, design methods based on alternative optimization objectives have been proposed. In [24] and [25], the peak voltage gain and current stress are considered in the selection of candidates. Designers can evaluate these results to identify the optimal design based on the specific requirements. In [26], the circulating energy is minimized to obtain best performance in the charging trajectory. In [27], the resonant root-mean-square (rms) current is employed as the optimization objective and algorithms, such as genetic algorithm, are used to find the solution.

For the three-phase *LLC* converter, the detailed model differs from that of the single-phase *LLC* converter due to coupling effects. The three-phase *LLC* converter has more complex-mode distributions, requiring comprehensive modeling to identify feasible modes for design. Specifically, unique conduction states caused by coupling effects occur when the secondary current is discontinuous, requiring thorough analysis. These differences mean that TDM-based design methods should be reconsidered for three-phase *LLC* converters. Currently, unlike single-phase *LLC* converters, limited research has been conducted. In [28], a design method is proposed to optimize the magnetic components for higher efficiency. However, the time-domain analysis is only partially utilized. Although piecewise equations are applied, current is approximated as a sinusoidal waveform. In [29], a TDM-based design method of three-phase Y-delta *LLC* converter is proposed for server power supply. However, due to the narrow voltage range of this application, the mode distribution is incomplete, making the design method unsuitable for battery chargers. The research in [30] extends modeling of the three-phase Y-delta *LLC* converter and proposes a design method aimed at higher power density. However, the operating mode distribution remains unclear, and efficiency optimization is not considered in the design. In conclusion, due to its high accuracy, TDM shows great potential for high-efficiency design of the three-phase *LLC* chargers. However, the existing TDM-based design methods for three-phase *LLC* converters are restricted to applications with narrow voltage ranges. New optimal design methods are needed to effectively improve the efficiency of three-phase *LLC* converters over a wide voltage range, as required in applications, such as battery chargers.

To address the above-mentioned issues, this article proposes a design method based on TDM for three-phase *LLC* chargers with higher analytical accuracy and power efficiency. The main contributions can be concluded as follows.

1) A comprehensive TDM of the three-phase *LLC* converter has been developed, providing detailed analysis of operating modes and mode distributions across the entire operating range for output characteristics, such as voltage gain and output power. TDM serves as a foundation for the proposed design method.
2) A design method aimed at enhancing efficiency across the entire charging process is proposed for three-phase *LLC* chargers. The proposed design method takes the resonant rms current as the optimization objective. Based on TDM, the relationship of the optimization objective and parameters is derived. A step-by-step design procedure is introduced to identify parameters that optimize resonant rms current across the charging process while simultaneously ensuring system specifications and soft switching. The proposed design method maximizes the converter's performance, thereby improving efficiency across the entire charging process.

The rest of this article is organized as follows. Section II establishes a complete TDM of the three-phase *LLC* converters and analyzes operating modes and mode distributions. Section III provides the optimal design methodology for three-phase *LLC* chargers. In Section IV, the accuracy and efficiency performance of the proposed design method is evaluated and analyzed through simulation and comparison. The experimental results are provided in Section V. Finally, Section VI concludes this article.

II. TDM of Three-Phase *LLC* Converter

A. Operating Principle

Fig. 1 illustrates the topology schematic of a three-phase *LLC* converter. The primary switches S_1–S_6 form an interleaved three-phase active bridge, while the secondary diodes D_1–D_6

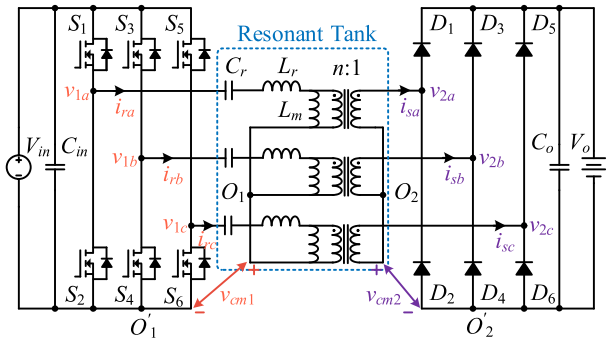

Fig. 1. Topology schematic of the three-phase *LLC* converter.

TABLE I
KEY PARAMETERS OF THREE-PHASE *LLC* CONVERTER

Parameter	Symbol and definition
Resonant frequency	$\omega_r = 1/\sqrt{L_r C_r} = 2\pi f_r$
Switching frequency	$f_s = 1/T_s$
Characteristic impedance	$Z_r = \sqrt{L_r/C_r}$
Inductor ratio	$k = L_m/L_r$
Voltage gain	$M = nV_o/V_{in}$

constitute a three-phase rectifier bridge. The resonant tank parameters between each phase are identical. L_r and C_r denote the resonant inductors and resonant capacitors, respectively, while L_m represents the magnetizing inductors of the transformers. Both the primary and secondary sides of transformers utilize the Y-connection. The turns ratio of transformers is n. v_{1x} and v_{2x} $(x = a, b, c)$ refer to the primary and secondary voltages of resonant tanks; i_{rx} and i_{sx} $(x = a, b, c)$ denote the primary and secondary currents of resonant tanks. In addition, v_{cm1} and v_{cm2} are the common-mode voltages. Table I lists the key parameters to describe the features of the converter. The switching frequency is defined as f_s. The resonant frequency f_r, inductor ratio k, and characteristic impedance Z_r uniquely determine the resonant elements L_r, C_r, and L_m. The voltage gain of the converter is defined as M.

For simplicity, several assumptions are made when analyzing the operating principle of the converter: First, all the components are considered ideal and the parasitic parameters are neglected; second, the filter capacitors C_{in} and C_o are sufficiently large to ensure that no high-frequency voltage ripples appear on the input and output sides. Fig. 2 depicts typical operating waveforms of a three-phase *LLC* converter in the below-resonance region (BRR) $(f_s < f_r)$ and above-resonance region (ARR) $(f_s > f_r)$. The primary switches are modulated by PFM and there is a symmetrical phase shift of 120° across three phase legs. The upper and lower switches of each phase are driven complementarily, allowing for adjustable switching frequency while maintaining a fixed duty cycle of 50%. It is beneficial to define the primary switching function $S_{1x}(t)$ $(x = a, b, c)$ for the three phase legs. $S_{1x}(t)$ equals 1 when the upper switch of a phase leg is ON and 0 when the lower switch is ON.

Before detailed modeling, three concepts are defined first in Table II, which are the operating mode, sector, and operating

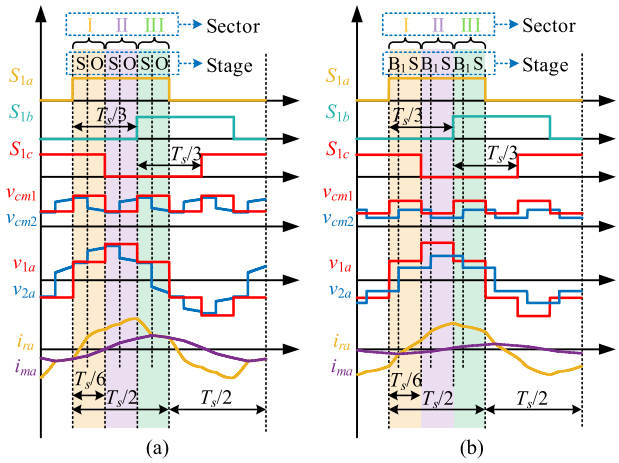

Fig. 2. Typical operating waveforms of three-phase *LLC* converter. (a) BRR. (b) ARR.

TABLE II
DEFINITION OF OPERATING MODE, SECTOR, AND OPERATING STAGE

Concept	Function	Time span
Operating mode	Describe characteristics of converter	$T_s/2$
Sector	Simplify the coupling effects	$T_s/6$
Operating stage	Categorize the conduction states of switches and diodes	$(0, T_s/6)$

stage. Operating modes describe the converter's steady-state characteristics over half a switching period, including resonant waveforms and indicators, such as voltage gain, zero-voltage switching (ZVS), and zero-current switching (ZCS) states. Sectors are employed to simplify the coupling effects. Taking the primary side as an example, the relationship between the resonant tank voltages and switching functions can be derived as follows:

$$v_{1x}(t) = V_{\mathrm{in}} S_{1x}(t) - v_{\mathrm{cm1}}(t), \ (x = a, b, c). \tag{1}$$

Due to the consistency of parameters, the waveforms of the three phases are identical, differing only by a 120° phase shift. The resonant tank voltages have a coupling relationship

$$v_{1a} + v_{1b} + v_{1c} = 0. \tag{2}$$

The common-mode voltage can be derived by combining (1) and (2)

$$v_{\mathrm{cm1}}(t) = (S_{1a}(t) + S_{1b}(t) + S_{1c}(t)) V_{\mathrm{in}}/3. \tag{3}$$

As illustrated in Fig. 2, $v_{\mathrm{cm1}}(t)$ is a square wave. In combination with (1), the resonant tank voltages are derived as step waves with the voltage of $\pm V_{\mathrm{in}}/3$ and $\pm 2V_{\mathrm{in}}/3$. There are three steps with a duration of $T_s/6$ in half a switching period, named as sectors I, II, and III. Due to the symmetry among the three phases, each sector shares similar operating principles and has the same operating stages. Therefore, analyzing one sector is sufficient, as the others can be deduced similarly.

TABLE III
DEFINITION AND NORMALIZATION OF VARIABLES

Base values	Symbol	Definition
Voltage	V_B	$V_B = V_{in}$
Impedance	Z_B	$Z_B = Z_r = \sqrt{L_r/C_r}$
Current	I_B	$I_B = V_B/Z_B$
Frequency	ω_B	$\omega_B = \omega_r = 2\pi f_r$
Parameter	**Symbol**	**Normalized variable**
Time	t	$\theta = \omega_B t$
Switching frequency	f_s	$f_n = f_s/f_r$
Resonant current	$i_{rx,\mathrm{XY}}$	$i^*_{rx,\mathrm{XY}} = i_{rx,\mathrm{XY}}/I_B$
Resonant voltage	$v_{rx,\mathrm{XY}}$	$v^*_{rx,\mathrm{XY}} = v_{rx,\mathrm{XY}}/V_B$
Magnetizing current	$i_{mx,\mathrm{XY}}$	$i^*_{mx,\mathrm{XY}} = i_{mx,\mathrm{XY}}/I_B$
Magnetizing voltage	$v_{mx,\mathrm{XY}}$	$v^*_{mx,\mathrm{XY}} = v_{mx,\mathrm{XY}}/V_B$
Primary resonant tank voltage	$v_{1x,\mathrm{XY}}$	$v^*_{1x,\mathrm{XY}} = v_{1x,\mathrm{XY}}/V_B$
Secondary resonant tank voltage	$v_{2x,\mathrm{XY}}$	$v^*_{2x,\mathrm{XY}} = v_{2x,\mathrm{XY}}/V_B$
Subscript of Symbol	**Definition**	**Variable**
x	Phase	a, b, c
X	Stage	S, A_1, A_2, B_1, B_2, O
Y	Sector	I, II, III

The operating stage is the most basic concept to distinguish the conduction states of the switches and diodes. There could be 1–3 stages in each sector. Detailed analysis of operating stages will be presented in Section II-B.

B. Operating Stages

The coupling effect results in a greater variety of operating stages for the three-phase *LLC* converter. The primary task is to systematically classify and model each of these operating stages. For a given converter, the operating stages vary with operating conditions, including the switching frequency and load. The operating stages are essentially distinguished by the conduction states of the primary switches and secondary diodes. These stages can be categorized into two groups: continuous conduction stage (CCS) and discontinuous conduction stage (DCS), determined by the continuity of the secondary current of the resonant tank. Before analysis, Table III defines the base values and unifies variables for the simplicity and consistency in the solutions.

1) Continuous Conduction Stage: In CCS, either the upper or lower diode of each secondary phase leg is always conducting, ensuring that each phase remains connected to the output side. To be more intuitive, the conduction states can be represented using space vector, as shown in Fig. 3(a). S_{1x} and S_{2x} ($x = a, b, c$) are the switching functions for the both sides, mentioned in Section II-A. There are six conduction states for each side, corresponding to vector u_1–u_6. For examples, u_1 indicates that S_1, S_4, and S_5 are ON, or D_1, D_4, and D_5 are ON. For phase A, the primary conduction states follow a conversion sequence from u_1 to u_6.

As illustrated in Fig. 3(b)–(d), the primary and secondary conduction states, u_{pri} and u_{sec}, could be different at the same time, resulting in five types of CCS. According to the relative position between u_{pri} and u_{sec}, these types are named as S, A_1, A_2, B_1, and B_2. S stage represents the stage where u_{pri} and u_{sec} are the same. A_1 or A_2 stage represents that u_{sec} leads u_{pri} for one or two state position. B_1 or B_2 stage indicates a lag of u_{sec} behind u_{pri} by one or two state position. Although u_{pri} and u_{sec} vary across different sectors, their relative positions can remain consistent. Therefore, conduction states in different sectors that share the same relative position are grouped into the same category to maintain clarity and consistency when modeling multiple stages. This indicates that each sector has the same stages. Fig. 4 presents a unified equivalent circuit of CCS, using phase A as an example. The state equations can be derived from this equivalent circuit as follows:

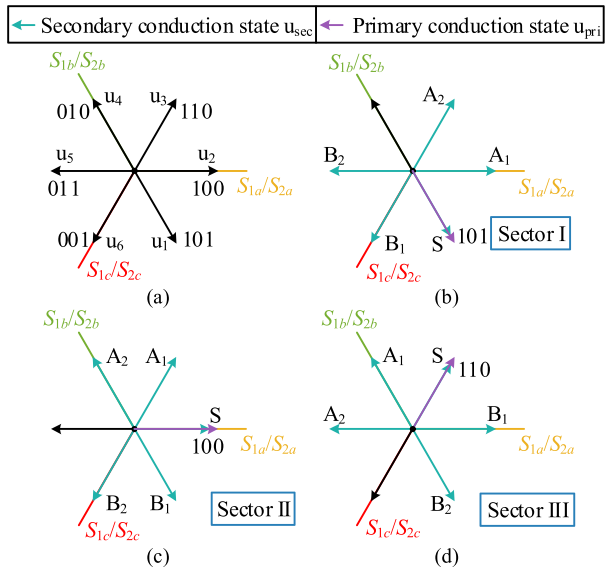

Fig. 3. CCS analysis for (a) definition of conduction states, and classification of CCS in (b) sector I, (c) sector II, and (d) sector III.

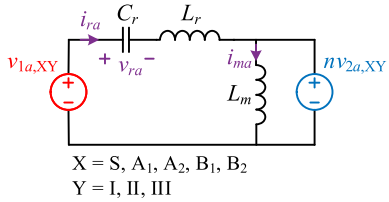

Fig. 4. Unified equivalent circuit of CCS for phase A.

$$\begin{cases} L_r \frac{di_{ra,\mathrm{XY}}}{dt} + v_{ra,\mathrm{XY}} = v_{1a,\mathrm{XY}} - n\, v_{2a,\mathrm{XY}} = \frac{pV_{\mathrm{in}}}{3} - \frac{qnV_o}{3} \\ C_r \frac{dv_{ra,\mathrm{XY}}}{dt} = i_{ra,\mathrm{XY}} \\ L_m \frac{di_{ma,\mathrm{XY}}}{dt} = \frac{qnV_o}{3} \end{cases} \tag{4}$$

where the combination of p and q specifies the primary and secondary voltages of resonant tank in different stages and sectors, as shown in Table XI of Appendix. After solving (4),

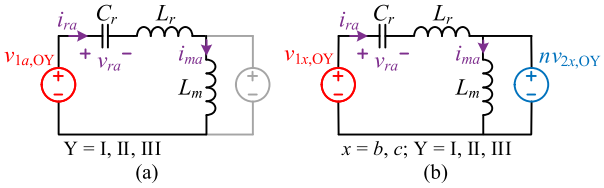

Fig. 5. Equivalent circuit when phase A is in DCS. (a) Phase A. (b) Phase B or phase C.

the normalized solutions can be derived as follows:

$$\begin{cases} v^*_{ra,\mathrm{XY}}(\theta) = V^*_{1ra,\mathrm{XY}}\cos\theta + V^*_{2ra,\mathrm{XY}}\sin\theta + \frac{p}{3} - \frac{qM}{3} \\ i^*_{ra,\mathrm{XY}}(\theta) = -V^*_{1ra,\mathrm{XY}}\sin\theta + V^*_{2ra,\mathrm{XY}}\cos\theta \\ i^*_{ma,\mathrm{XY}}(\theta) = I^*_{1ma,\mathrm{XY}} + \frac{qM}{3k}\theta,\ \theta\in[0,\theta_X] \end{cases} \tag{5}$$

where $V^*_{1ra,\mathrm{XY}}$, $V^*_{2ra,\mathrm{XY}}$, and $I^*_{1ma,\mathrm{XY}}$ are unknown normalized initial values of solutions. The time domain of each stage is defined as [0, θ_X] for simplicity, where θ_X is the normalized time span of stage X.

2) Discontinuous Conduction Stage: In DCS, neither the upper nor lower diode of the phase with discontinuous secondary current is conducting. The DCS can, thus, be denoted as O stage due to the OFF state of diodes. For example, when phase A is in DCS, it cannot transfer power to the output side, so the magnetizing inductor will participate in the resonance. The other two phases can transfer power, but they are coupled with phase A. Fig. 5 shows the equivalent circuit of DCS. The state equations of phase A can be formulated as follows:

$$\begin{cases} v^*_{ra,\mathrm{OY}}(\theta) = V^*_{1ra,\mathrm{OY}}\cos(k_1\theta) + V^*_{2ra,\mathrm{OY}}\sin(k_1\theta) + \alpha/3 \\ i^*_{ra,\mathrm{OY}}(\theta) = -k_1V^*_{1ra,\mathrm{OY}}\sin(k_1\theta) + k_1V^*_{2ra,\mathrm{OY}}\cos(k_1\theta) \\ v^*_{ma,\mathrm{OY}}(\theta) = -kk_1^2V^*_{1ra,\mathrm{OY}}\cos(k_1\theta) - kk_1^2V^*_{2ra,\mathrm{OY}}\sin(k_1\theta) \end{cases} \tag{6}$$

where $k_1 = 1/\sqrt{k+1}$. α specifies the values of v_{1a} for different sectors. Due to the coupling relationship between the three phases, the operating principles of the other two phases differ from those in the CCS. The secondary resonant tank voltage can be derived similar to the primary side by using (1) and (2)

$$\begin{cases} v_{\mathrm{cm2}} = \frac{1}{2}(v_{2a,\mathrm{OY}} + (S_{2b}+S_{2c})V_o) = \frac{1}{2}\left(\frac{v_{ma,\mathrm{OY}}}{n} + V_o\right) \\ v_{2x,\mathrm{OY}} = S_{2x}V_o - v_{\mathrm{cm2}} = -\frac{1}{2}\frac{v_{ma,\mathrm{OY}}}{n} + \tau\frac{V_o}{2},(x=b,c) \end{cases} \tag{7}$$

where $\tau = \pm 1$ is determined by the conduction states of diodes in phase B or C. Then, the normalized solutions of the other two phases can be deduced as follows:

$$\begin{cases} v^*_{rx,\mathrm{OY}}(\theta) = V^*_{1rx,\mathrm{OY}}\cos(\theta) + V^*_{2rx,\mathrm{OY}}\sin(\theta) \\ +\frac{1}{2}V^*_{1ra,\mathrm{OY}}\cos(k_1\theta) + \frac{1}{2}V^*_{2ra,\mathrm{OY}}\sin(k_1\theta) + \frac{\beta}{3} + \tau\frac{M}{2} \\ i^*_{rx,\mathrm{OY}}(\theta) = -V^*_{1rx,\mathrm{OY}}\sin(\theta) + V^*_{2rx,\mathrm{OY}}\cos(\theta) \\ -\frac{k_1}{2}V^*_{1ra,\mathrm{OY}}\sin(k_1\theta) - \frac{k_1}{2}V^*_{2ra,\mathrm{OY}}\cos(k_1\theta) \\ i^*_{mx,\mathrm{OY}}(\theta) = I^*_{1mx,\mathrm{OY}} + \frac{M}{2k}\theta + \frac{k_1}{2}V^*_{1ra,\mathrm{OY}}\sin(k_1\theta) \\ -\frac{k_1}{2}V^*_{2ra,\mathrm{OY}}\cos(k_1\theta) \end{cases} \tag{8}$$

TABLE IV
SOLVING CONSTRAINTS OF OPERATING MODES

Constraint	Expression
Continuity	$\begin{cases} v^*_{ra,\mathrm{X_1Y_1}}(\theta_{\mathrm{X_1}}) = v^*_{ra,\mathrm{X_2Y_2}}(0) \\ i^*_{ra,\mathrm{X_1Y_1}}(\theta_{\mathrm{X_1}}) = i^*_{ra,\mathrm{X_2Y_2}}(0) \\ i^*_{ma,\mathrm{X_1Y_1}}(\theta_{\mathrm{X_1}}) = i^*_{ma,\mathrm{X_2Y_2}}(0) \end{cases}$
Symmetry	$\begin{cases} v^*_{ra,\mathrm{X_1I}}(0) = -v^*_{ra,\mathrm{X_2III}}(\theta_{\mathrm{X_2}}) \\ i^*_{ra,\mathrm{X_1I}}(0) = -i^*_{ra,\mathrm{X_2III}}(\theta_{\mathrm{X_2}}) \\ i^*_{ma,\mathrm{X_1I}}(0) = -i^*_{ma,\mathrm{X_2III}}(\theta_{\mathrm{X_2}}) \end{cases}$
Output current	$I^*_o = \frac{I_oZ_r}{V_{in}} = \frac{3nf_n}{\pi}\sum_{\mathrm{Y}}\int_0^{\theta_\mathrm{X}}\lvert i^*_{ra,\mathrm{XY}} - i^*_{ma,\mathrm{XY}}\rvert d\theta$

where β denotes the values of v_{1a} for phase B or C. $V^*_{1rx,\mathrm{OY}}$, $V^*_{2rx,\mathrm{OY}}$, and $I^*_{1mx,\mathrm{OY}}$ are unknown normalized initial values of solutions. The operating states (α, β, τ) of different phases and sectors are presented in Table XII of Appendix.

C. Analysis and Distribution of Operating Modes

After modeling all stages, the operating modes and their distributions can be analyzed. The sequence of stages in each sector is consistent. Therefore, all modes are named according to the sequence of stages.

When solving operating modes, several types of constraints need to be considered, as outlined in Table IV. The first constraint is continuity: the capacitor voltage and inductor current at the boundaries of adjacent stages must be continuous. The second constraint is symmetry: in steady-state conditions, the initial values of the capacitor voltage and inductor current should be the inverse of their final values over half a switching period. The third constraint establishes a relationship between the inductor current and the output power, which can be derived from the output current. By integrating these constrains into one nonlinear system of equations, the operating modes can be solved. SO mode in Fig. 2(a) is taken as an example to demonstrate the equation set constructed by these constrains. The equations based on the continuity constraints can be derived as follows:

$$\begin{cases} v^*_{ra,\mathrm{SI}}(\theta_S) = v^*_{ra,\mathrm{OI}}(0), i^*_{ra,\mathrm{SI}}(\theta_S) = i^*_{ra,\mathrm{OI}}(0) \\ v^*_{ra,\mathrm{OI}}(\theta_O) = v^*_{ra,\mathrm{SII}}(0), i^*_{ra,\mathrm{OI}}(\theta_O) = i^*_{ra,\mathrm{SII}}(0) \\ v^*_{ra,\mathrm{SII}}(\theta_S) = v^*_{ra,\mathrm{OII}}(0), i^*_{ra,\mathrm{SII}}(\theta_S) = i^*_{ra,\mathrm{OII}}(0) \\ v^*_{ra,\mathrm{OII}}(\theta_O) = v^*_{ra,\mathrm{SIII}}(0), i^*_{ra,\mathrm{OII}}(\theta_O) = i^*_{ra,\mathrm{SIII}}(0) \\ v^*_{ra,\mathrm{SIII}}(\theta_S) = v^*_{ra,\mathrm{OIII}}(0), i^*_{ra,\mathrm{SIII}}(\theta_S) = i^*_{ra,\mathrm{OIII}}(0) \\ i^*_{ma,\mathrm{SI}}(\theta_\mathrm{S}) = i^*_{ma,\mathrm{OI}}(0), i^*_{ma,\mathrm{OI}}(\theta_\mathrm{O}) = i^*_{ma,\mathrm{SII}}(0) \\ i^*_{ma,\mathrm{SII}}(\theta_\mathrm{S}) = i^*_{ma,\mathrm{OII}}(0), i^*_{ma,\mathrm{OII}}(\theta_\mathrm{O}) = i^*_{ma,\mathrm{SIII}}(0) \\ i^*_{ma,\mathrm{SIII}}(\theta_\mathrm{S}) = i^*_{ra,\mathrm{OIII}}(0) \end{cases} \tag{9}$$

where θ_S and θ_O are the duration of S stage and O stage.

Then, the symmetry constraints are listed as follows:

$$\begin{cases} v^*_{ra,\mathrm{SI}}(0) = v^*_{ra,\mathrm{OIII}}(\theta_\mathrm{O}), i^*_{ra,\mathrm{SI}}(0) = i^*_{ra,\mathrm{OIII}}(\theta_\mathrm{O}) \\ i^*_{ma,\mathrm{SI}}(0) = i^*_{ma,\mathrm{OIII}}(\theta_\mathrm{O}). \end{cases} \tag{10}$$

The final one is the output current constraint

$$I^*_o = \frac{I_oZ_B}{V_{in}} = \frac{3nf_n}{\pi}\int_0^{\theta_\mathrm{S}}\left(i^*_{ra,\mathrm{SII}}(\theta) - i^*_{ma,\mathrm{SII}}(\theta)\right)d\theta\#$$

TABLE V
OPERATING MODES AND CHARACTERISTICS

	f_n <1										
Mode	A_1A_2	A_1OA_2	A_1O	A_1	SA_1	OA_1	OA_1O	SOA_1	SO	OSO	O
Voltage Gain	$M<1$		$M<1/M>1$			$M>1$					
ZCS	×	√	√	×	×	√	√	√	√	√	OFF
	f_n =1			f_n >1							
Mode	S	OSO	O	O	OSO	OS	B_1OS	B_1S	B_1	B_2B_1	
Voltage Gain	$M=1$	$M>1$		$M>1$		$M<1$					
ZCS	×	√	OFF	OFF	√	√	√	×	×	×	

$$+\frac{3nf_n}{\pi}\int_0^{\theta_O}\left(i^*_{ra,\mathrm{OII}}(\theta)-i^*_{ma,\mathrm{OII}}(\theta)\right)d\theta. \tag{11}$$

Besides, θ_S and θ_O have the relationship as follows:

$$\theta_S+\theta_O=\pi/3f_n. \tag{12}$$

By combining (9)–(12), a solvable system of 19 equations with 19 unknown variables is established. Since the equations are nonlinear and transcendental, only numerical solutions can be obtained. The MATLAB function "lsqnonlin" can be used to compute the numerical solutions. When focusing on the operating conditions and resonant parameters, the process of solving the equation set can be expressed in a straightforward and intuitive form

$$M=g_P\left(k,Z_r,f_n,I_o\right) \tag{13}$$

where g_P represents the process of solving the equation set at operating point P. For these five variables, if any four of them are known, the remaining one can be solved. Since only numerical solutions are available, g_P does not have an analytical expression.

Through a combination of theoretical analysis and simulation, 17 operating modes have been identified under different operating conditions, with 11 in BRR and 7 in ARR. Table V presents the operating modes and their basic characteristics. The OSO and O modes appear in the entire frequency range, while S mode appears only when $f_n=1$. ZCS can be judged by the presence of O stage. When O stage occurs in a given mode, the secondary current drops to zero before the diodes turn OFF. Therefore, ZCS is achieved, eliminating the reverse recovery losses.

To determine the mode of a given operating point, it is necessary to calculate the mode boundary first as the condition for judgment. The mode boundary refers to the transition point between two adjacent operating modes, which is a special case of one operating mode. For example, the boundary between SO and SOA_1 mode occurs in SO mode when v_{ma} equals $-nV_o/3$ at the end of O stage. By incorporating this additional constraint into the equation set, the mode boundary can be solved. According to (13), with the existence of additional constraint, the output current constraint is no longer needed. This means that the mode boundary is determined only by the resonant tank parameters, independent of the power load. Key mode boundaries and their constraints are summarized in Table VI. By solving all mode boundaries, the overall characteristics of the converter can be obtained. For example, Fig. 6 illustrates the mode distributions across the entire M-f_n plane.

TABLE VI
KEY MODE BOUNDARIES AND CONSTRAINTS

Boundary	Mode	Constraint
SO/OSO	SO	$i^{*\prime}_{ra,\mathrm{SI}}(0)=i^{*\prime}_{ma,\mathrm{SI}}(0)=M/3k$
SO/SOA_1	SO	$v^*_{ma,\mathrm{OIII}}(\theta_{\mathrm{OIII}})=-M/3$
SA_1/SOA_1	SA_1	$i^{*\prime}_{ra,A_1\mathrm{III}}(0)=i^{*\prime}_{ma,A_1\mathrm{III}}(0)=-M/3k$
SOA_1/OA_1O	OA_1	$v^*_{ma,\mathrm{OIII}}(\theta_{\mathrm{OIII}})=-M/3$
B_1S/B_1OS	B_1S	$i^{*\prime}_{ra,\mathrm{SI}}(0)=i'_{ma,\mathrm{SI}}(0)=M/3k$
OSO/B_1OS	OS	$v^*_{ma,\mathrm{OI}}(\theta_{\mathrm{OI}})=M/3$

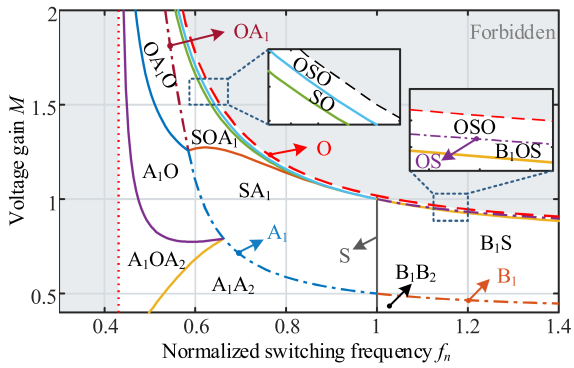

Fig. 6. Mode distribution in M–f_n plane.

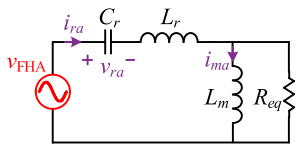

Fig. 7. Equivalent circuit of FHA model.

D. Comparison Between TDM and FHA Model

This section compares and analyzes TDM and the FHA model from theoretical perspective. The FHA model only considers the fundamental harmonic and neglects the higher order harmonics. Fig. 7 presents the equivalent circuit of the FHA model [7]. The input side of the resonant tank is driven by a sinusoidal voltage source, and the rectifier on the output side is modeled as

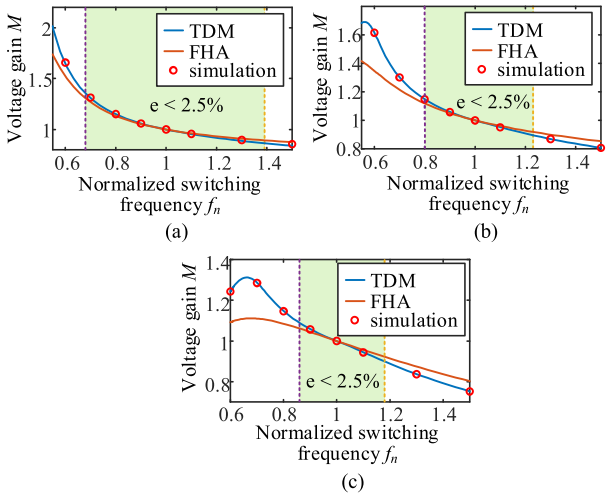

Fig. 8. Theoretical voltage gain comparison of TDM, FHA, and simulation with different Q. (a) $Q = 0.2$. (b) $Q = 0.5$. (c) $Q = 0.8$.

a resistor. The equivalent resistance can be derived as follows:

$$R_{\text{eq}} = \frac{6n^2 R_o}{\pi^2} = \frac{6n^2 V_o}{\pi^2 I_o} \tag{14}$$

where R_o is the load resistor. Based on the equivalent circuit, the voltage gain expression for FHA model can be deduced as

$$M_{\text{FHA}} = \frac{1}{\sqrt{\left(1 + \frac{1}{k} - \frac{1}{k f_n^2}\right)^2 + \frac{\pi^4 Q^2}{36 n^4}\left(f_n - \frac{1}{f_n}\right)^2}} \tag{15}$$

where $Q = Z_r / R_o$ represents the quality factor, serving as a measure of the load. It can be concluded that the voltage gain correlates with the resonant tank parameters and operating conditions. According to (15), when f_n and Q are fixed, the peak voltage gain increases in BRR as k decreases. A smaller k implies a smaller magnetizing inductance when Q remains constant, typically resulting in a larger peak magnetizing current and a larger resonant current.

Fig. 8 compares the voltage gain of the TDM and FHA model with the ideal simulation results under different Q. The accuracy of the FHA model decreases significantly when the switching frequency deviates from the resonant frequency. Specifically, the voltage gain is lower than the simulation results in BRR and higher in ARR. This discrepancy arises due to the approximation inherent in the FHA model. Therefore, k is designed to be smaller to achieve a wider voltage gain range, resulting in underutilization of the resonant tank. Moreover, a smaller k will increase the resonant current, hence increasing the losses. The feasible working range can be evaluated based on the model's error. In Fig. 8, it can be observed that the feasible range of the FHA model is consistently narrow, regardless of the load. Therefore, the FHA model is unsuitable for the charger design.

In contrast, the voltage gain calculated by the TDM matches the simulation results across all cases. The mechanism of the TDM proves that there is no approximation in the modeling process. It accurately solves all the operating modes and describes their distributions. The TDM can describe the output characteristics across the entire working range, so it is a better choice for charger design.

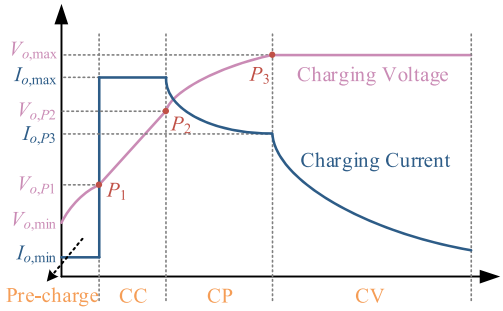

Fig. 9. Charging profile of EV battery.

III. Design Methodology

This section introduces a novel design method to enhance the efficiency across the entire charging range of the three-phase *LLC* charger. By combining the TDM and the charging trajectory, suitable operating modes for each charging pattern are selected to meet the system specifications and soft-switching constraints. The resonant rms current is selected as the optimization objective, and its relationship with design parameters is researched under entire charging process. Then, a step-by-step design procedure is proposed to determine the optimal parameters.

A. Operating Mode Selection

Fig. 9 presents the charging profile of the EV battery. It contains four charging patterns: precharge pattern, constant current (CC) pattern, constant power (CP) pattern, and constant voltage (CV) pattern. During the precharge pattern, the charging voltage remains low, while the charging current is typically 10% of the rated current. In the CP pattern, the power reaches its rated level, and the voltage continues to increase. In the CV pattern, the current decreases until it reaches its minimum. Operating points P_1, P_2, and P_3 represent the boundaries between adjacent charging patterns.

Soft switching is crucial for maintaining high efficiency in three-phase *LLC* converters. Well-designed parameters can ensure ZVS of the primary switches and ZCS of the secondary diodes throughout the entire charging process. ZCS was analyzed in Section II, while this part will analyze the constraints for ZVS. The TDM is employed to analyze the ZVS states for each operating mode. Appropriate operating modes are then selected to ensure ZVS of the entire charging process. Achieving ZVS requires that the resonant current can fully charge or discharge the output capacitor of the primary switches during the dead time, expressed as follows:

$$|i_{r0}^*| \geq |i_{r,\text{ZVS}}^*| = \frac{2C_{oss}V_{\text{in}}}{t_d I_B} = \frac{2C_{oss}Z_r}{t_d} \tag{16}$$

where i_{r0}^* is the resonant current when switches turn ON. $i_{r,\text{ZVS}}^*$ represents the critical resonant current required to achieve ZVS. C_{oss} is the output capacitance of the primary switches, and t_d is

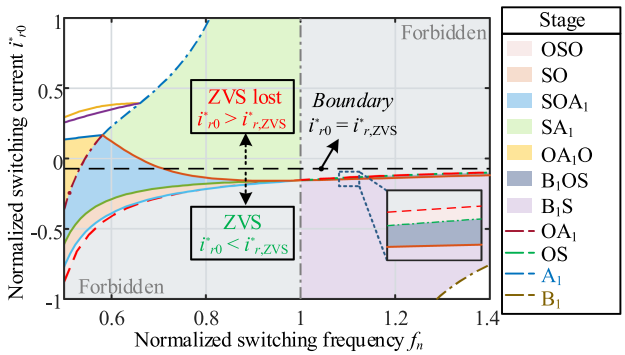

Fig. 10. Mode distribution in i^*_{r0}–f_n plane for the upper switches.

TABLE VII
APPROPRIATE OPERATING MODES FOR EACH CHARGING PATTERN

Charging pattern	Operating mode
Pre-charge	OSO, B_1OS, B_1S
CC/CP/CV	OSO, SO, SOA_1, OA_1O

the dead time. Fig. 10 illustrates the mode distribution in i^*_{r0}–f_n plane for the upper switches. Modes below the boundary $i^*_{r,\mathrm{ZVS}}$ can achieve ZVS. Meanwhile, the forbidden region refers to operating conditions the converter cannot achieve even under zero load. It is evident that nearly all modes in ARR can achieve ZVS. ZVS may only be lost when the switching frequency is high, and the load reaches its minimum. As for BRR, modes OSO, OS, SOA_1, OA_1O, and SA_1 can realize ZVS. Furthermore, modes that can achieve both ZVS and ZCS are OSO, OS, SOA_1, and OA_1O in BRR, while in ARR, they are OSO and B_1OS.

The appropriate modes are selected for each charging pattern. The precharge pattern, characterized by low voltage gain and output current, is reasonably set in ARR for two reasons. First, the use of ARR can expand the operating range and maximize the converter's performance. Second, it sets the boundary frequency between the precharge and CC patterns equal to the resonant frequency, thereby minimizing the impact of the power load jump between these two patterns. OSO and B_1OS modes in ARR can be used as they achieve both ZVS and ZCS. The B_1S mode can also be considered due to its little impact from ZCS. The other three charging patterns are set in the BRR for their higher voltage gain. In conclusion, the mode candidates for each charging pattern are listed in Table VII.

B. Optimization Objective

As demonstrated in the existing research, the efficiency of *LLC* converters is closely related to the resonant rms current $I_{r,\mathrm{rms}}$ [22], [24]. A lower $I_{r,\mathrm{rms}}$ results in reduced losses, ultimately improving the efficiency. Therefore, $I_{r,\mathrm{rms}}$ is selected as the optimization objective to evaluate the efficiency. This section establishes the relationship between $I_{r,\mathrm{rms}}$ and design parameters, and proposes the optimization objective under the entire charging process.

$I_{r,\mathrm{rms}}$ can be calculated based on the waveform in positive half switching period

$$I_{r,\mathrm{rms}} = I_B \sqrt{\frac{1}{\theta_0} \sum\nolimits_{\mathrm{Y}} \sum\nolimits_{\mathrm{X}} \int_0^{\theta_{\mathrm{X}}} i^{*2}_{r,\mathrm{XY}}(\theta)\, d\theta} \tag{17}$$

where θ_0 denotes the normalized time of half switching period and θ_{X} denotes the normalized time span of stage X. $I_{r,\mathrm{rms}}$ is dependent on the operating conditions, including voltage gain M, output current I_o, and switching frequency f_n, as well as resonant tank parameters k and Z_r. Since there is no analytical solution, the relationship can be expressed as follows:

$$I_{r,\mathrm{rms}} = \Gamma(k, Z_r, M, I_o, f_n). \tag{18}$$

According to the analysis of (13), when four parameters are specified, the remaining one can be solved. For a given operating point P, M, and I_o are fixed. Therefore, parameters f_n, k, and Z_r have the relationship described as follows:

$$Z_r = g_P(k, f_n). \tag{19}$$

Then, by combining (18) and (19), the rms current of operating point P is only related to k and f_n

$$I_{r,\mathrm{rms},P} = \Gamma(k, Z_r, M_P, I_{o,P}, f_n) = \Gamma_P(k, f_n). \tag{20}$$

To satisfy the design requirement for minimum frequency limit $f_{n,\mathrm{llim}}$, the minimum switching frequency $f_{n,\mathrm{min}}$ should be determined. The local optimization objective will be derived based on the analysis of finding the k to minimize $I_{r,\mathrm{rms}}$ with fixed f_n. Then, the global optimization objective will be analyzed through the relationship between the local optimal solution and f_n.

1) Local Optimization Objective: Since CC, CP, and CV patterns are crucial for efficiency performance, the relationship between $I_{r,\mathrm{rms}}$ and k is investigated in BRR. To intuitively analyze the relationship, the schematic trajectories of these three patterns are presented in the mode distribution of normalized power p^* and switching frequency f_n in Fig. 11. There is a nonmonotonic relationship between the p^* and M, where p^* initially increases and then decreases as M increases at specific f_n. As a result, the mode distributions in p^*–f_n plane are divided into two parts: the negative correlation plane where p^* decreases monotonically as M increases [see Fig. 11(a)], and the positive correlation plane where p^* increases monotonically as M increases [see Fig. 11(b)]. The ZVS boundary (p^*_{ZVS}) is also marked in two planes. Most of the negative correlation plane can achieve ZVS, while most of the positive correlation plane cannot. Therefore, the three charging patterns should be set in the negative correlation plane to ensure ZVS operation.

For any operating point P with a fixed f_n in Fig. 11(a), as k increases, the relative position of P will move downward from SOA_1 mode to SO mode, away from the p^*_{ZVS}, which means the ZVS margin ($i^*_{r0}/i^*_{r,\mathrm{ZVS}}$) increases. The relationship between $I_{r,\mathrm{rms},P}$ and ZVS margin is illustrated in Fig. 12. With fixed f_n, $I_{r,\mathrm{rms},P}$ increases as the ZVS margin increases (with k increasing). From a physical perspective, a larger ZVS margin implies a larger i^*_{r0}, resulting in increased resonant rms current and losses. Therefore, it can be concluded that, for any operating point,

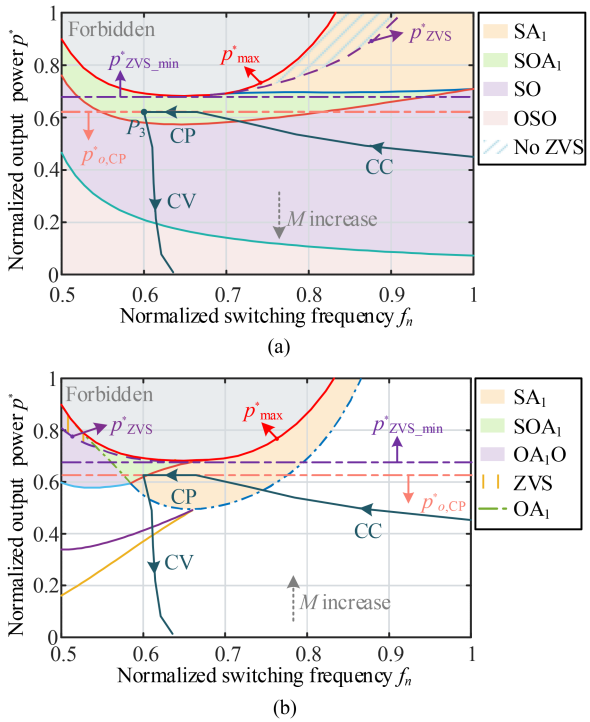

Fig. 11. Mode distribution in p^*–f_n plane. (a) Negative correlation plane. (b) Positive correlation plane.

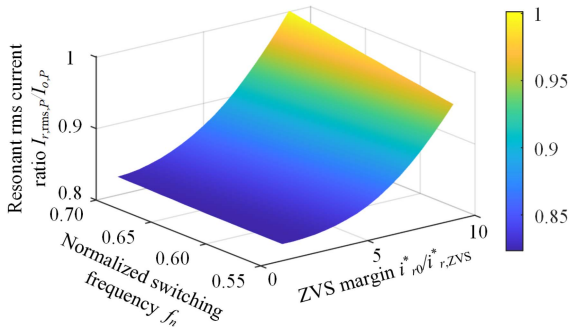

Fig. 12. Resonant rms current versus ZVS margin with different f_n.

moving it closer to ZVS boundary p^*_{ZVS} reduces its resonant rms current. Furthermore, when applying this principle to the charging patterns, the optimal choice is to make the CP pattern $p^*_{o,CP}$ tangent to p^*_{ZVS}, which ensures that the entire pattern is closest to the ZVS boundary. In addition, as shown in Fig. 11(a), p^*_{ZVS} is smaller than the power limit p^*_{max}, indicating that the charging profile will not exceed the converter's power limit. The local optimization objective can be expressed as follows:

$$\begin{cases} p^*_{diff} = p^*_{ZVS,min} - p^*_{o,CP} = h\ (k_s, Z_{rs}) = 0 \\ p^*_{ZVS,min} = \min\{p^*_{ZVS}\},\ p^*_{o,CP} = P_{rate}/\left(V^2_{in}/Z_r\right) \end{cases} \tag{21}$$

where p^*_{diff} denotes the relative position between $p^*_{ZVS,min}$ and $p^*_{o,CP}$. h represents the relationship between p^*_{diff} and parameters k and Z_r. k_s and Z_{rs} are the solutions of $p^*_{diff} = 0$. Since there are infinite solutions for (21), the operating point P_3 is selected as the anchor point for CP pattern, as shown in Fig. 11(a). As

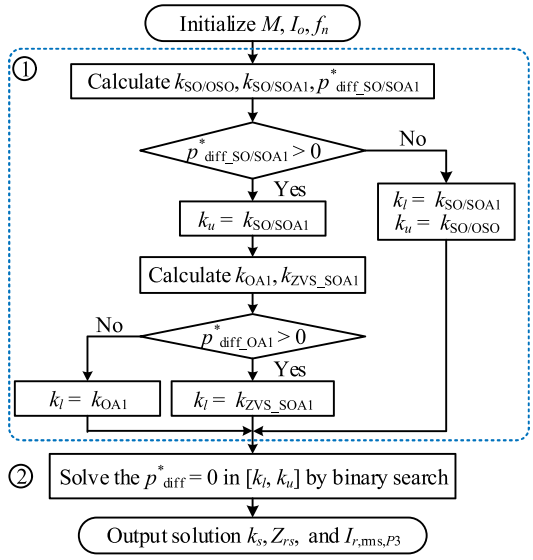

Fig. 13. Solving process of k_s for local optimal solution with given f_n.

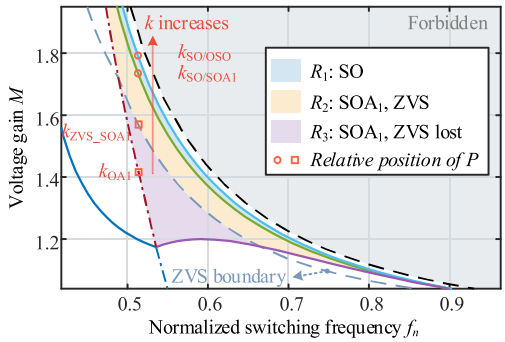

Fig. 14. Relative position of operating point P_3 as k increases in M–f_n plane.

the boundary point between CP and CV patterns, P_3 has the minimum switching frequency $f_{n,min}$ and the maximum voltage gain M_{max}, both of which are fixed and must be satisfied in the design process. With the anchor point P_3, the local optimal objective in (21) can be derived as follows:

$$\begin{cases} Z_{rs} = g_{P3}\left(k_s, f_{n,min}\right) \\ p^*_{diff} = h\left(k_s, g_{P3}\left(k_s, f_{n,min}\right)\right) = 0. \end{cases} \tag{22}$$

The local optimization objective is to determine k_s for a given $f_{n,min}$ such that $p^*_{diff} = 0$. Fig. 13 presents the process of solving for k_s. The first part is to determine the solution domain. It is intuitive to examine the trends of relative position between $p^*_{ZVS,min}$ and $p^*_{o,CP}$ with varying k in the M–f_n mode distribution plane, as shown in Fig. 14. According to (22), relative position p^*_{diff} can be calculated through the anchor point P_3. As k increases, P_3 will move through several key mode boundaries (OA$_1$, SO/SOA$_1$, and SO/OSO). Since mode boundaries have additional constraint, the value of k and p^*_{diff} at these mode boundaries can be calculated directly and be used to define the limits of the solution domain. The upper limit of solution domain is easily determined by evaluating the p^*_{diff} at boundary of SO

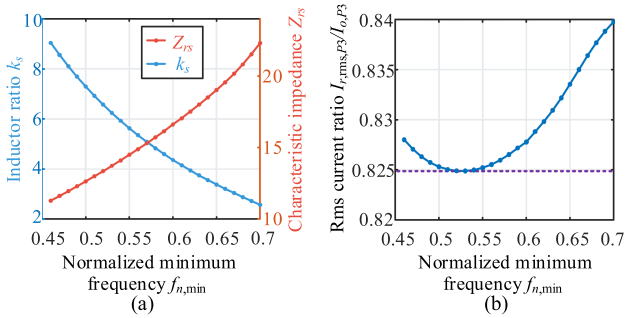

Fig. 15. Local optimal design results with different $f_{n,\min}$. (a) k_s and Z_{rs}. (b) $I_{r,\text{rms},P3}$.

TABLE VIII
SYSTEM SPECIFICATIONS OF THREE-PHASE *LLC* CHARGER

Parameter	Value
Power rating P_{rate}	4.5 kW
Input voltage V_{in}	400 V
Output voltage $V_{o,\min}$-$V_{o,\max}$	280-450 V
Resonant frequency f_r	50 kHz
Switching frequency range $f_{s,\text{llim}}$-$f_{s,\text{ulim}}$	30-75 kHz
Boundary of pre-charge and CC $V_{o,P1}$	300 V
Boundary of CC and CP $V_{o,P2}$	375 V

and SOA_1. Similarly, the lower limit can be obtained from the OA_1 mode boundary or ZVS boundary in SOA_1 mode. After determining the solution domain, the next part is to solve for k_s within this domain, using the binary search method.

2) Global Optimization Objective: After finding the local optimal solution with fixed $f_{n,\min}$, the global optimization objective can be obtained by analyzing the relationship between the local optimal solution and $f_{n,\min}$. The resonant rms current of P_3 ($I_{r,\text{rms},P3}$) is used to evaluate the rms current performance across the charging process, which can be calculated by

$$I_{r,\text{rms},P3} = \Gamma_{P3}\ (k_s, f_{n,\min}) = \Gamma_{P3}\ (f_{n,\min})\,. \tag{23}$$

Fig. 15 provides the changing trends of k_s, Z_{rs}, and $I_{r,\text{rms},P3}$ with $f_{n,\min}$. As Fig. 15(a) illustrates, when $f_{n,\min}$ increases, k_s decreases, while Z_{rs} increases. This monotonic relationship is helpful for solving process. As shown in Fig. 15(b), $I_{r,\text{rms},P3}$ has a minimum value. Therefore, the global optimization objective is to find $f_{n,\min}$ to minimize $I_{r,\text{rms},P3}$ while satisfying all the constraints. The solving process will be discussed in Section III-C.

C. Design Procedure

This section presents a step-by-step design procedure, as depicted in Fig. 16. Each step will be discussed in detail as follows.

Step 1. System specifications: The first step is to determine the system specifications. This design procedure takes a 4.5-kW three-phase *LLC* charger as an example, and the key design specifications are listed in Table VIII. The t_d and C_{oss} can be determined after selecting the switches.

Step 2. Design transformer turns ratio: According to the analysis in Section III-A, the precharge pattern is set in ARR,

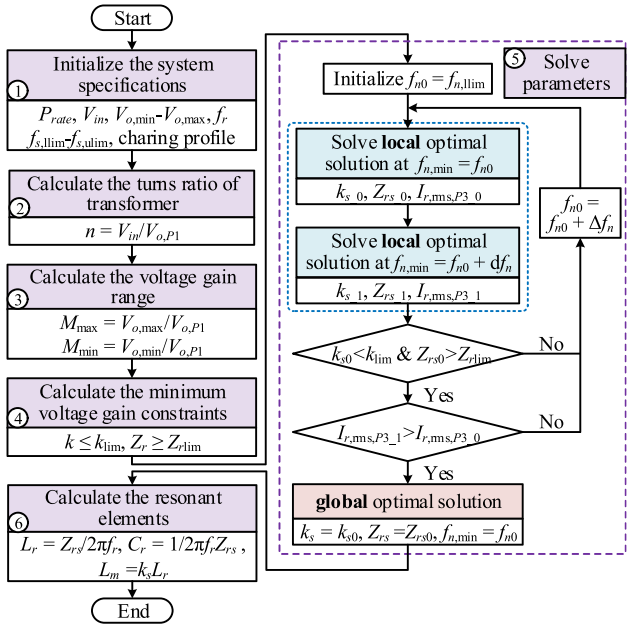

Fig. 16. Design flowchart of the proposed method.

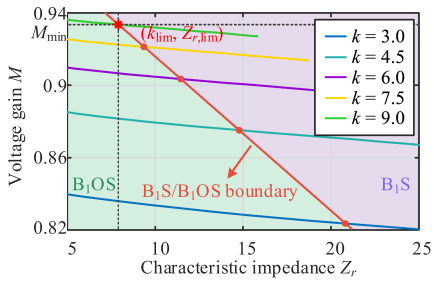

Fig. 17. Voltage gain with k and Z_r when $f_n = f_{n,\text{ulim}}$ and $I_o = I_{o,\min}$.

while the other patterns are set in BRR. Therefore, the boundary of the precharge pattern and the CC pattern P_1 is set at $f_n = 1$. The turns ratio of transformers can be calculated as follows:

$$n = V_{\text{in}}/V_{o,P1}. \tag{24}$$

Step 3. Calculate the voltage gain range: After determining the turns ratio, the voltage gain range can be derived as follows:

$$\begin{cases} M_{\max} = V_{o,\max}/V_{o,P1} \\ M_{\min} = V_{o,\min}/V_{o,P1}. \end{cases} \tag{25}$$

Step 4. Minimum voltage gain constraints: At the start of the precharge pattern, the voltage gain and output current reach their minimum, and the output power is very low. To meet the minimum voltage gain ($M_{\min}$) requirement, the voltage gain at $f_{n,\max}$ must be less than $M_{\min}$ when the output current is $I_{o,\min}$. Fig. 17 illustrates the relationship between M and the parameters k and Z_r when $f_n = f_{n,\text{ulim}}$ and $I_o = I_{o,\min}$. As k decreases and Z_r increases, M decreases, making it easier to satisfy the constraint. In addition, to ensure ZCS of the secondary diodes, it is advisable to avoid B_1S mode if possible. Consequently, the parameter limits are defined where the voltage gain at B_1S/B_1OS

boundary equals $M_{\min}$, marked by "$*$" in Fig. 17. The parameter limits $k_{\lim}$ and $Z_{r,\lim}$ can be obtained. To satisfy the $M_{\min}$ requirement, k_s should be smaller than $k_{\lim}$ and Z_{rs} should be larger than $Z_{r,\lim}$, which can be expressed as follows:

$$\begin{cases} (k_{\lim}, Z_{r,\lim}) = g_{\mathrm{B_1S/B_1OS}}\ (M_{\min}, I_{o,\min}, f_{n,\mathrm{ulim}}) \\ k_s \le k_{\lim} \\ Z_{rs} \ge Z_{r,\lim} \end{cases} \tag{26}$$

where $g_{\mathrm{B_1S/B_1OS}}$ represents the process of solving the equation set at $\mathrm{B_1S/B_1OS}$ boundary, similar to (13).

Step 5. Solve parameters: This step describes the process to find the global optimal solution. The global optimal objective is to find the minimum $I_{r,\mathrm{rms},P3}$ while satisfying all the solving constraints. There are three inequality constraints. The first one is that $f_{n,\min}$ should be greater than the provided lower frequency limit $f_{n,\mathrm{llim}}$. The other two constraints are derived from step 4, which can also be equalized to the switching frequency constraints based on Fig. 15(a). The solving expression is given as follows:

$$\begin{cases} \min\ I_{r,\mathrm{rms},P3} = \Gamma_{P3}\ (f_{n,\min}) \\ f_{n,\min} \ge\ f_{n,\mathrm{llim}} = f_{s,\mathrm{llim}}/f_r \\ k_s \le k_{\lim} \Rightarrow f_{n,\min} \ge f_{n,\mathrm{lim1}} \\ Z_{rs} \ge Z_{r,\lim} \Rightarrow f_{n,\min} \ge f_{n,\mathrm{lim2}} \end{cases} \tag{27}$$

where $f_{n,\mathrm{lim1}}$ and $f_{n,\mathrm{lim2}}$ are the equivalent frequencies. The solving process, as illustrated in Fig. 16, is described as follows.

1) First, f_{n0} is defined as the solving point of $f_{n,\min}$ in each iteration. At the beginning of the solving process, it is initialized to the provided lower frequency limit $f_{n,\mathrm{llim}}$.
2) Next, set $f_{n,\min}$ to f_{n0} and $f_{n0} + \Delta f_n$ to solve the local optimal solutions based on the objective in (22), obtaining k_s, Z_{rs}, and $I_{r,\mathrm{rms},P3}$, respectively. Δf_n represents the iteration step, which can be set as 0.005.
3) After obtaining the two sets of parameters, the minimum voltage gain constraints from Step 4 should be evaluated. If the constraints are satisfied, the solving process moves to 4). Otherwise, the process continues with the next iteration.
4) After the minimum voltage gain constraints are satisfied, the minimum $I_{r,\mathrm{rms},P3}$ will be evaluated. If the minimum current is achieved, the solving process is over. Otherwise, the next iteration is performed.

Step 6. Calculate resonant elements: After solving the k_s and Z_{rs}, the resonant elements can be calculated as follows:

$$\begin{cases} L_r = Z_{rs}/2\pi f_r \\ C_r = 1/2\pi f_r Z_{rs} \\ L_m = k_s\, L_r. \end{cases} \tag{28}$$

IV. Performance Comparison and Analysis

To validate the proposed design method, a comparison is conducted between this method and other design methods. The system specifications are already provided by Table VIII. The primary switch is selected as CI60N120SM, and C_{oss} can be calculated to be 400 pF. Considering the switching frequency and characteristics of switches, t_d is designed as 350 ns. Table IX lists the design results. The first set of parameters is designed by using the proposed method (Method I). The second set of parameters is also obtained through the proposed method, but the calculation is implemented based on the FHA model (Method II). The last set is designed by a traditional FHA-based method (Method III) [17]. This method selects one appropriate set of parameters based on the constraints of voltage gain, power load, and minimum switching frequency. However, these design constraints are not optimal for the efficiency. According to Table IX, it can be concluded that the FHA-based design methods have a smaller k than that of the proposed TDM-based design method. This proves that the low accuracy of FHA model reduces the utilization of resonant tank, hence undermining the efficiency.

TABLE IX
Parameter Design Results of Three Design Methods

Parameter	I. Proposed method	II. Proposed method based on FHA	III. FHA-based method from [17]
L_r	57.13 μH	53.14 μH	63.66 μH
C_r	177.34 nF	190.68 nF	159.15 nF
L_m	256.58 μH	203.95 μH	171.89 μH
k	4.4908	3.8383	2.7
Z_r	17.9490	16.6931	20

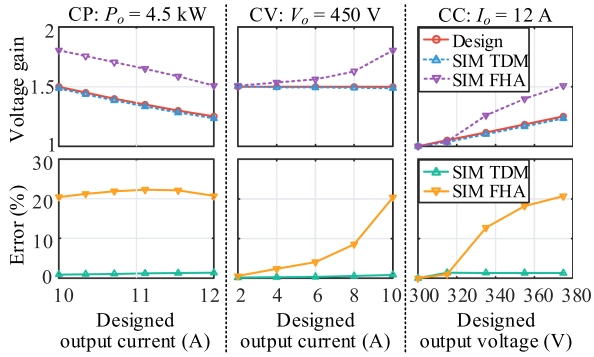

Fig. 18. Voltage gain comparison between the theory and simulation of TDM-based and FHA-based design methods.

A. Accuracy Comparison

Methods I and II in Table IX are selected for the accuracy comparison between the TDM-based and FHA-based design methods. The comparison is made on several key operating points under CC, CP, and CV patterns. The comparison method is described as follows. First, based on the designed output voltage and current, calculate the theoretical switching frequency of each operating point by TDM and FHA model, respectively. Then, by combining the switching frequency and designed output current, perform simulations to obtain the actual output voltages and compare them with the designed values. The simulation will consider the parasitic parameters. The comparison results are shown in Fig. 18. The proposed TDM-based design method is highly precise across a wide range of output voltages and currents, with the voltage gain error consistently remaining below 1%. The error is mainly caused by the parasitic resistance. In contrast, the FHA-based design method exhibits poor accuracy at operating

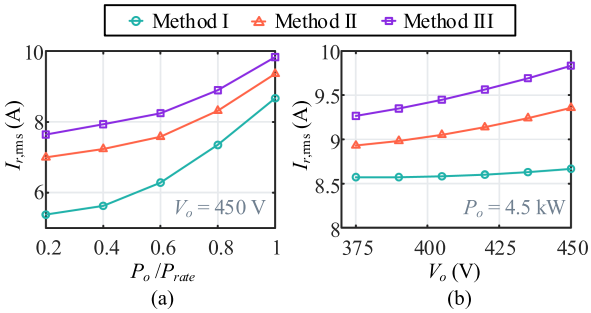

Fig. 19. Resonant rms current comparison between three design methods. (a) CV stage. (b) CP stage.

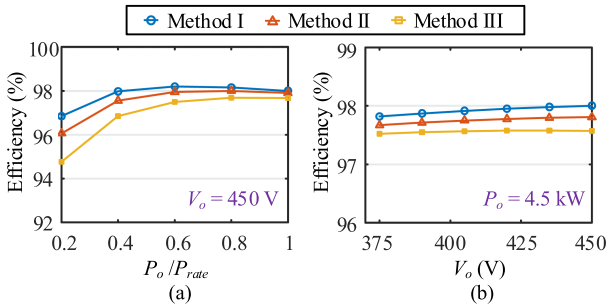

Fig. 20. Theoretical efficiency comparison between three design methods. (a) CV stage. (b) CP stage.

points with high voltage gain, with errors exceeding 20% at most. The FHA model has acceptable accuracy only under the light-load conditions or when the switching frequency is close to the resonant frequency. At most operating points, the simulation voltage gains obtained by FHA-based design method are much higher than the designed values. This phenomenon proves that the FHA-based design method fails to fully exploit the potential of the resonant tank, leading to a higher resonant rms current at the same operating point. Therefore, the TDM-based design method is more accurate than the FHA-based design method for the three-phase *LLC* charger design.

B. Resonant rms Current and Efficiency Comparison

The resonant rms current and efficiency for three design methods in Table IX are calculated and compared. Fig. 19 illustrates the comparison of resonant rms current in CV and CP patterns. In CV pattern, the output voltage is fixed at the maximum output voltage $V_o = 450$ V, and in CP pattern, the output power is fixed at the rated power $P_o = 4.5$ kW. It can be observed that the resonant rms current of the proposed method is the lowest in all charging patterns. This proves that the proposed TDM-based design method effectively optimizes the rms current across the entire charging range, allowing for the full utilization of resonant tank. Furthermore, the rms current of the method III is the largest, with an increase of up to 25% at most. This indicates that the poor accuracy of the FHA-based design method leads to a higher rms current.

The efficiency is calculated based on the power loss model provided by Deng et al. [26]. Fig. 20 presents the efficiency of three design methods across different charging patterns. When combined with Fig. 19, a consistent trend is observed between the efficiency and the resonant rms current. This indicates that the efficiency is mainly influenced by the resonant rms current. Fig. 20 shows that the proposed method has the highest efficiency, while the FHA-based method in [17] has the lowest efficiency. The results prove that the proposed TDM-based design method enhances the efficiency throughout the entire charging process.

Fig. 21 illustrates the power loss distribution of three design methods at several key operating points. The losses related to resonant rms current dominate the total losses. When the resonant rms current is optimized, the efficiency can be significantly

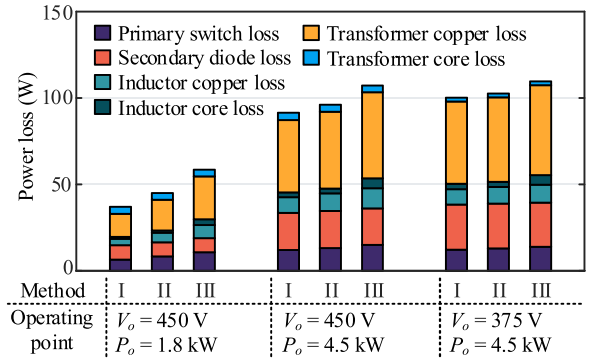

Fig. 21. Power losses of three design methods at key operating points.

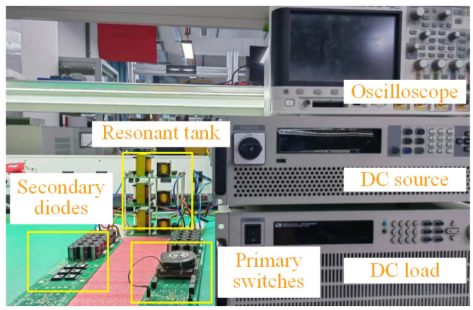

Fig. 22. Experimental setup.

enhanced. Therefore, taking the resonant rms current to estimate the loss is reasonable. The comparison results validate that the proposed design method can improve the efficiency of entire charging process.

Table X compares proposal with other design methods for three-phase *LLC* converters. It can be observed that other TDM-based methods focus on the application of narrow voltage gain and no optimization methods are proposed. The proposed method (in bold in Table X) has the highest efficiency due to the optimization based on TDM.

V. Experiment

To validate the effectiveness of the proposed design method, an experimental setup rated at 4.5 kW was established based on the parameters in Tables VIII and IX. Fig. 22 demonstrates a photograph of the experimental setup.

TABLE X
COMPARISON BETWEEN DIFFERENT DESIGN METHODS FOR THREE-PHASE *LLC* CONVERTERS

Method	Model	Application	Gain range	Optimization objective	Peak efficiency	Full-load efficiency
[28]	FHA	Battery charger	1.31	Magnetic elements	/	/
[17]	FHA	Battery charger	3	/	96.7% @ 2.3kW	95.8kW @ 3.8kW
[29]	TDM	Server power supply	1	/	97.5% @ 3kW	96.1% @ 5kW
[30]	TDM	Aircraft's electrical system	1.21	/	96.5% @ 1kW	/
Proposed	TDM	Battery charger	1.6	Resonant rms current	**98.1% @ 2.7kW**	**97.8% @ 4.5kW**

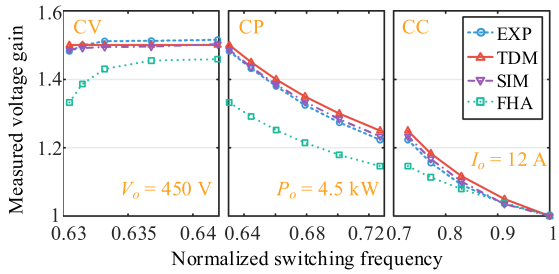

Fig. 23. Voltage gain comparison among experiment, simulation, and theory in CV, CP, and CC stage.

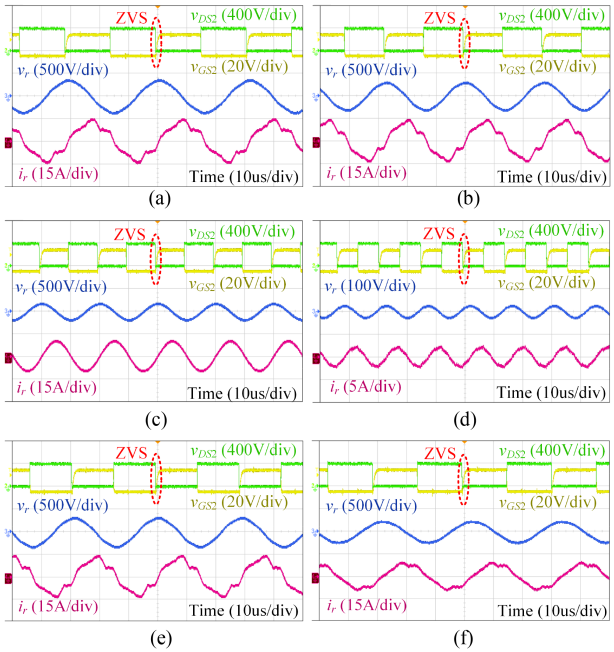

Fig. 24. Experimental waveforms of key operating points. (a) $V_o = 450$ V and $I_o = 10$ A. (b) $V_o = 375$ V and $I_o = 12$ A. (c) $V_o = 300$ V and $I_o = 12$ A. (d) $V_o = 280$ V and $I_o = 1.2$ A. (e) $V_o = 400$ V and $I_o = 11.25$ A. (f) $V_o = 450$ V and $I_o = 5$ A.

A. *Voltage Gain Results*

The voltage gain of the proposed method is measured on the experimental setup to verify the accuracy of the TDM. Fig. 23 illustrates the comparison results of voltage gain at specific operating points among the experiment, simulation, TDM, and FHA model. At each operating point, the output current is predetermined, and the switching frequency is calculated by the TDM. Then, the same switching frequency and output current are set in the experiment, simulation, and theory models for each specific operating point to obtain its voltage gain. The voltage gains at key operating points under the CV, CP, and CC patterns are compared. The results from the experiment, simulation, and TDM match closely across the entire charging range. The discrepancy between the experimental and theoretical results is mainly caused by the parasitic parameters, which are not considered in the TDM theory. However, the voltage gains predicted by the FHA model diverge severely from the other results, especially in CV and CP patterns, where the switching frequency deviates from the resonant frequency. The FHA model is only accurate near the resonant frequency in the CC pattern. The comparison reveals that TDM is highly accurate across the entire charging patterns, whereas the FHA model is unable to provide a precise description in the wide voltage range application. Therefore, the accurate TDM is more suitable for the optimal parameter design of the three-phase *LLC* converter

B. *Key Operating Waveforms*

Fig. 24 illustrates the key waveforms at specific operating points of the proposed method, including the driving voltage and drain–source voltage of the switch, resonant current, and resonant voltage. Fig. 24(a) shows the waveforms at boundary operating point between CP and CV patterns, operating in SOA_1 mode. Fig. 24(b) presents the boundary points between the CP and CC patterns, operating in SO mode. Fig. 24(c) depicts the boundary point of CC pattern and precharge pattern, where the converter operates at the resonant frequency and the resonant current is sinusoidal. Fig. 24(d) shows the initial point in precharge pattern, where the output voltage and current are at their lowest. Specifically, Fig. 24(e) demonstrates the operating point where ZVS is nearly the hardest to realize in CP pattern. Finally, Fig. 24(f) shows the half-load operating point in CV pattern. The lower switch in phase A is chosen to verify the realization of ZVS. It can be observed that, at all the operating points in Fig. 24, the drain–source voltage falls to zero before the switch is turned ON. Therefore, ZVS is realized in all operating conditions, which validates the effectiveness of the design methodology and guarantees the efficiency.

Moreover, Fig. 25 presents a comparison of the resonant current waveforms from the experiment, simulation, and theoretical analysis. The results indicate that the waveforms closely match throughout most of the switching period. The largest deviation occurs at the stage when the secondary current is discontinuous. At this stage, the equivalent output capacitors of diodes join the resonance, causing the oscillation of resonant current. Since our model does not account for this output capacitor, it cannot

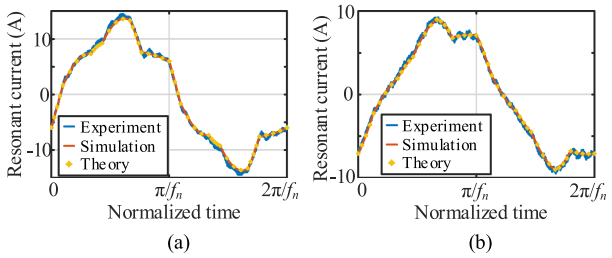

Fig. 25. Waveform comparison among experiment, simulation, and theory at key operating points. (a) $V_o = 450$ V and $I_o = 10$ A. (b) $V_o = 450$ V and $I_o = 5$ A.

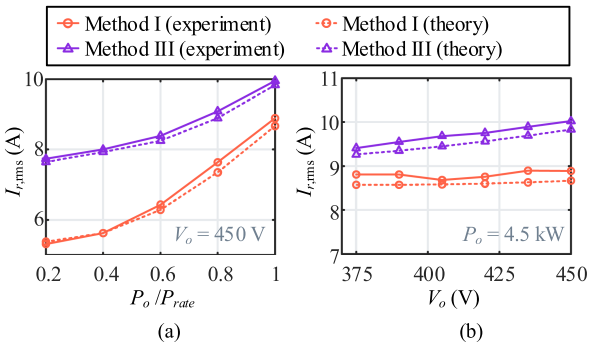

Fig. 26. Resonant rms current comparison between experiment and theory. (a) CP stage. (b) CV stage.

describe this oscillation accurately. However, the impact of the output capacitor on the converter's operation is acceptable.

C. Resonant rms Current and Efficiency Measurement

The resonant rms current of Methods I (Proposed) and III is measured and compared with their simulation results, as shown in Fig. 26. The experimental results exhibit trends that are consistent with the simulations. In addition, the discrepancies between the experimental and simulation results are within an acceptable range, with errors not exceeding 3%. $I_{r,\mathrm{rms}}$ of the proposed method is lower than that of the FHA-based method, demonstrating the effectiveness of the current optimization.

Finally, the efficiency of Methods I (Proposed) and III under various operating points is measured and compared with the theoretical results, as shown in Fig. 27. The measured efficiency of the proposed design method is higher than that of FHA-based method, which proves that the proposed method enhances the efficiency of the three-phase *LLC* charger across the entire charging range. The experimental results closely match the theoretical results, with a maximum error of less than 0.14%, which is within an acceptable range. This discrepancy is probably caused by nonlinearity of parameters, rms current calculation errors, and inaccuracies in loss models. Moreover, the trends of the experimental and theoretical efficiency curves are nearly identical. Therefore, the theoretical loss model is effective enough to evaluate the efficiency performance.

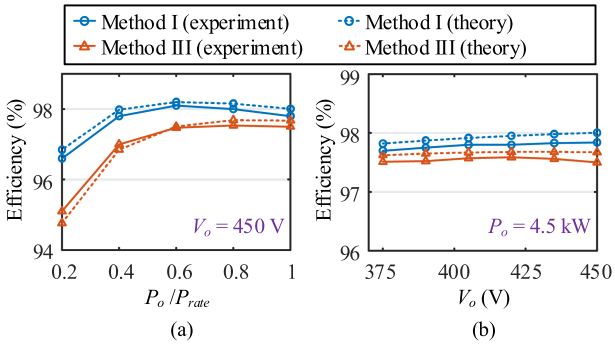

Fig. 27. Efficiency comparison between experiment and theory. (a) CP stage. (b) CV stage.

TABLE XI
OPERATING STATES OF DIFFERENT STAGES AND SECTORS IN CCS

Sector Y	(p, q) of stage X				
	S	A_1	A_2	B_1	B_2
I	(1, 1)	(1, 2)	(1, 1)	(1, -1)	(1, -2)
II	(2, 2)	(2, 1)	(2, -1)	(2, 1)	(2, -1)
III	(1, 1)	(1, -1)	(1, -2)	(1, 2)	(1, 1)

TABLE XII
OPERATING STATES OF DIFFERENT PHASES AND SECTORS IN DCS

Sector Y of phase A	(α, β, τ)	
	Phase B	Phase C
I	(1, -2, -1)	(1, 1, 1)
II	(2, -1, -1)	(2, -1, 1)
III	(1, 1, -1)	(1, -2, 1)

VI. CONCLUSION

This article proposed a TDM-based design methodology for three-phase *LLC* chargers to enhance the accuracy and efficiency throughout the entire working range. First, a comprehensive TDM for the three-phase *LLC* converter is established. The operating modes and mode distributions across the entire operating range are well modeled. Then, based on the TDM, a design method is proposed to enhance the efficiency by optimizing the resonant rms current across the entire charging process. Through a step-by-step design procedure, the system specifications and soft switching can be realized. Finally, the simulation, experiment, and comparison are conducted to verify the proposed design method. The results show that the proposed design method has better accuracy and efficiency performance across the entire charging process compared with the FHA-based design methods, and the peak efficiency can reach 98.1%.

APPENDIX

For CCS, the values of the primary and secondary resonant tank voltages vary in different stages and sectors. p and q in (5) are used to specify the concrete values, as shown in Table XI.

For DCS, when phase A is discontinuous, (α, β, τ) in (8) and (9) is used to specify the concrete values of primary and secondary resonant tank voltages of three phases, as shown in Table XII.

REFERENCES

[1] A. Khaligh and M. D'Antonio, "Global trends in high-power on-board chargers for electric vehicles," *IEEE Trans. Veh. Technol.*, vol. 68, no. 4, pp. 3306–3324, Apr. 2019.

[2] F. Musavi, M. Craciun, D. S. Gautam, W. Eberle, and W. G. Dunford, "An LLC resonant DC–DC converter for wide output voltage range battery charging applications," *IEEE Trans. Power Electron.*, vol. 28, no. 12, pp. 5437–5445, Dec. 2013.

[3] Y. Wei, Q. Luo, X. Du, N. Altin, A. Nasiri, and J. M. Alonso, "A dual half-bridge LLC resonant converter with magnetic control for battery charger application," *IEEE Trans. Power Electron.*, vol. 35, no. 2, pp. 2196–2207, Feb. 2020.

[4] H. Wang and Z. Li, "A PWM LLC type resonant converter adapted to wide output range in PEV charging applications," *IEEE Trans. Power Electron.*, vol. 33, no. 5, pp. 3791–3801, May 2018.

[5] N. Shafiei, M. Ordonez, M. Craciun, C. Botting, and M. Edington, "Burst mode elimination in high-power LLC resonant battery charger for electric vehicles," *IEEE Trans. Power Electron.*, vol. 31, no. 2, pp. 1173–1188, Feb. 2016.

[6] H. Li et al., "A bidirectional synchronous/asynchronous rectifier control for wide battery voltage range in SiC Bidirectional LLC chargers," *IEEE Trans. Power Electron.*, vol. 37, no. 5, pp. 6090–6101, May 2022.

[7] S. A. Arshadi, M. Ordonez, W. Eberle, M. Craciun, and C. Botting, "Three-phase LLC battery charger: Wide regulation and improved light-load operation," *IEEE Trans. Power Electron.*, vol. 36, no. 2, pp. 1519–1531, Feb. 2021.

[8] J. Guan et al., "A high efficiency Δ-Lr-Y type three-phase interleaved LLC converter with less transformer loss," *IEEE Trans. Power Electron.*, vol. 38, no. 9, pp. 11152–11168, Sep. 2023.

[9] M. S. Almardy and A. K. S. Bhat, "Three-phase (LC)(L)-type series resonant converter with capacitive output filter," *IEEE Trans. Power Electron.*, vol. 26, no. 4, pp. 1172–1183, Apr. 2011.

[10] Y. Nakakohara, H. Otake, T. M. Evans, T. Yoshida, M. Tsuruya, and K. Nakahara, "Three-phase LLC series resonant DC/DC converter using SiC MOSFETs to realize high-voltage and high-frequency operation," *IEEE Trans. Ind. Electron.*, vol. 63, no. 4, pp. 2103–2110, Apr. 2016.

[11] R. Gadelrab and F. C. Lee, "PCB-based magnetic integration and design optimization for three-phase LLC," *IEEE Trans. Power Electron.*, vol. 38, no. 11, pp. 14037–14049, Nov. 2023.

[12] H. Wouters and W. Martinez, "Bidirectional onboard chargers for electric vehicles: State-of-the-art and future trends," *IEEE Trans. Power Electron.*, vol. 39, no. 1, pp. 693–716, Jan. 2024.

[13] B. Lu, W. Liu, Y. Liang, F. C. Lee, and J. D. van Wyk, "Optimal design methodology for LLC resonant converter," in *Proc. IEEE Appl. Power Electron. Conf. Expo.*, 2006, pp. 533–538.

[14] J. Deng, S. Li, S. Hu, C. C. Mi, and R. Ma, "Design methodology of LLC resonant converters for electric vehicle battery chargers," *IEEE Trans. Veh. Technol.*, vol. 63, no. 4, pp. 1581–1592, May 2014.

[15] R. Beiranvand, B. Rashidian, M. R. Zolghadri, and S. M. H. Alavi, "A design procedure for optimizing the LLC resonant converter as a wide output range voltage source," *IEEE Trans. Power Electron.*, vol. 27, no. 8, pp. 3749–3763, Aug. 2012.

[16] D. R. Linares, A. D. Expósito, and M. Vasić, "High-gain high-frequency three-phase LLC resonant converter design based on the wye–delta transformer for aircraft applications," *IEEE Trans. Power Electron.*, vol. 39, no. 4, pp. 4367–4383, Apr. 2024.

[17] X. Zhou et al., "A high-efficiency high-power-density on-board low-voltage DC–DC converter for electric vehicles application," *IEEE Trans. Power Electron.*, vol. 36, no. 11, pp. 12781–12794, Nov. 2021.

[18] H. Xu, Z. Yin, Y. Zhao, and Y. Huang, "Accurate design of high-efficiency LLC resonant converter with wide output voltage," *IEEE Access*, vol. 5, pp. 26653–26665, 2017.

[19] R. Yu, G. K. Y. Ho, B. M. H. Pong, B. W.-K. Ling, and J. Lam, "Computer-aided design and optimization of high-efficiency LLC series resonant converter," *IEEE Trans. Power Electron.*, vol. 27, no. 7, pp. 3243–3256, Jul. 2012.

[20] Y. Wei, Q. Luo, Z. Wang, and H. A. Mantooth, "A complete step-by-step optimal design for LLC resonant converter," *IEEE Trans. Power Electron.*, vol. 36, no. 4, pp. 3674–3691, Apr. 2021.

[21] M. F. Menke, J. P. Duranti, L. Roggia, F. E. Bisogno, R. V. Tambara, and Á. R. Seidel, "Analysis and design of the LLC LED driver based on state-space representation direct time-domain solution," *IEEE Trans. Power Electron.*, vol. 35, no. 12, pp. 12686–12701, Dec. 2020.

[22] Z. Fang, T. Cai, S. Duan, and C. Chen, "Optimal design methodology for LLC resonant converter in battery charging applications based on time-weighted average efficiency," *IEEE Trans. Power Electron.*, vol. 30, no. 10, pp. 5469–5483, Oct. 2015.

[23] G. A. Mudiyanselage, K. Kozielski, and A. Emadi, "Optimal LLC converter design with topology morphing control for wide voltage range battery charging applications," *IEEE Open J. Power Electron.*, vol. 5, pp. 1209–1226, Aug. 2024.

[24] Z. Hu, L. Wang, H. Wang, Y.-F. Liu, and P. C. Sen, "An accurate design algorithm for LLC resonant converters—Part I," *IEEE Trans. Power Electron.*, vol. 31, no. 8, pp. 5435–5447, Aug. 2016.

[25] Z. Hu, L. Wang, Y. Qiu, Y.-F. Liu, and P. C. Sen, "An accurate design algorithm for LLC resonant converters—Part II," *IEEE Trans. Power Electron.*, vol. 31, no. 8, pp. 5448–5460, Aug. 2016.

[26] J. Deng, C. C. Mi, R. Ma, and S. Li, "Design of LLC resonant converters based on operation-mode analysis for level two PHEV battery chargers," *IEEE/ASME Trans. Mechatron.*, vol. 20, no. 4, pp. 1595–1606, Aug. 2015.

[27] Y. Wei, T. Pereira, Y. Pan, M. Liserre, F. Blaabjerg, and H. A. Mantooth, "A general and automatic RMS current oriented optimal design tool for LLC resonant converters," *IEEE J. Emerg. Sel. Topics Power Electron.*, vol. 10, no. 6, pp. 7318–7332, Dec. 2022.

[28] A. Lordoglu, M. O. Gulbahce, D. A. Kocabas, and S. Dusmez, "Design and optimization of three-phase LLC charger with $\Delta - \Delta$ winding configuration," in *Proc. 48th Annu. Conf. IEEE Ind. Electron. Soc.*, 2022, pp. 1–6.

[29] K.-H. Chen, J.-Y. Lin, Y.-F. Lin, Y.-C. Chang, and H.-J. Chiu, "Design of three phase wye-delta LLC converter with time domain analysis," in *Proc. 10th Int. Conf. Power Electron. ECCE Asia*, 2019, pp. 1–6.

[30] A. de Juan, D. Serrano, P. Alou, J.-N. Mamousse, R. Denéieport, and M. Vasic, "Analytical modelling of single-phase and three-phase DC/DC LLC converters," in *Proc. IEEE Appl. Power Electron. Conf. Expo.*, 2022, pp. 2106–2113.

[31] M. Mu and F. C. Lee, "Design and optimization of a 380–12 V high-frequency, high-current LLC converter with GaN devices and planar matrix transformers," *IEEE J. Emerg. Sel. Topics Power Electron.*, vol. 4, no. 3, pp. 854–862, Sep. 2016.

[32] X. Pan, H. Li, Y. Liu, T. Zhao, C. Ju, and A. K. Rathore, "An overview and comprehensive comparative evaluation of current-fed-isolated-bidirectional DC/DC converter," *IEEE Trans. Power Electron.*, vol. 35, no. 3, pp. 2737–2763, Mar. 2020.

Ning Guo (Graduate Student Member, IEEE) received the B.S. degree in electrical engineering in 2021 from Xi'an Jiaotong University, Xi'an, China, where he is currently working toward the Ph.D. degree in electrical engineering.

His current research interests include topology, control, and design of isolated dc–dc converters.

Jinjun Liu (Fellow, IEEE) received the B.S. and Ph.D. degrees in electrical engineering from Xi'an Jiaotong University (XJTU), Xi'an, China, in 1992 and 1997, respectively.

He then joined Electrical Engineering School, XJTU, as a faculty. From late 1999 to early 2002, he was with the Center for Power Electronics Systems, Virginia Polytechnic Institute and State University, Blacksburg, VA, USA, as a Visiting Scholar. In late 2002, he was promoted to a Full Professor and then the Head of the Power Electronics and Renewable Energy Center, XJTU, which now comprises nearly 30 faculty members and around 300 graduate students and carries one of the leading power electronics' programs in China. From 2005 to early 2010, he served as an Associate Dean of Electrical Engineering School, XJTU, and from 2009 to early 2015, the Dean for Undergraduate Education of XJTU. He is currently an XJTU Distinguished Professor of power electronics. He coauthored 3 books (including one textbook), published more than 500 technical papers in peer-reviewed journals and conference proceedings, holds over 70 invention patents (China/US/EU), and delivered for many times plenary keynote speeches and tutorials at IEEE conferences or China national conferences. His research interests include modeling, control, and design methods and reliability evaluation and monitoring for power converters and electronified power systems, power quality control and utility applications of power electronics, and microgrid techniques for sustainable energy and distributed generation.

Dr. Liu was a recipient of many times governmental awards at national level or provincial/ministerial level for scientific research/teaching achievements, the 2006 Delta Scholar Award, the 2014 Chang Jiang Scholar Award, the 2014 Outstanding Sci-Tech Worker of the Nation Award, the 2016 State Council Special Subsidy Award, the IEEE Transactions on Power Electronics 2016 and 2021 Prize Paper Awards, the Nomination Award for the Grand Prize of 2020 Bao Steel Outstanding Teacher Award, and the 2022 Fok Ying Tung Education and Teaching Award. He served as the IEEE Power Electronics Society Region 10 Liaison and then China Liaison for 10 years, has been an Associate Editor for the IEEE TRANSACTIONS ON POWER ELECTRONICS since 2006, and 2015–2021 Vice President of IEEE PELS. He was on the Board of China Electrotechnical Society 2012–2020 and was elected the Vice President in 2013 and the Secretary General in 2018 of the CES Power Electronics Society. He was 2013–2021 Vice President for International Affairs, China Power Supply Society (CPSS), and since 2016, the inaugural Editor-in-Chief for *CPSS Transactions on Power Electronics and Applications*. He was elected the President of CPSS in November 2021. Since 2013, he has been serving as the Vice Chair of the Chinese National Steering Committee for College Electric Power Engineering Education Programs.

Sixing Du (Member, IEEE) received the B.S. degree from the Taiyuan University of Science and Technology, Taiyuan, China, in 2009, and the M.S. and Ph.D. degrees from Xi'an Jiaotong University, Xi'an, China, in 2011 and 2014, respectively, all in electrical engineering.

He is currently an Associated Professor with Xi'an Jiaotong University. From 2015 to 2019, he was a Postdoctoral Research Fellow with the Department of Electrical and Computer Engineering, Toronto Metropolitan University, Toronto, Canada, and the University of Toronto, Toronto, Canada, respectively. His research interests include high-power convers and their applications to medium-voltage motor drives and power systems.

Cong Li (Student Member, IEEE) received the B.S. degree in electrical engineering from Northwest Polytechnic University, Shaanxi, China, in 2018. He is currently working toward the Ph.D. degree in electrical engineering with Xi'an Jiaotong University, Xi'an, China.

His current research includes the topology and control of multiport converters, and wide range dc–dc converters.

Hui Chen (Student Member, IEEE) received the B.S. degree in electrical engineering and automation from Dalian Maritime University, Dalian, China, in 2016, and the M.S. and Ph.D. degrees in electrical engineering from the School of Electrical Engineering, Xi'an Jiaotong University, Xi'an, China, in 2019 and 2024, respectively.

In the same year, he joined Delta Electronics, Inc. His current research interests include power electronic transformer, bidirectional isolated dc–dc converters topology, multiphase VRM, and control techniques.

Zhifeng Deng (Graduate Student Member, IEEE) received the B.S. and M.S. degrees in electrical engineering in 2019 and 2022, respectively, from Xi'an Jiaotong University, Xi'an, China, where he is currently working toward the Ph.D. degree in electrical engineering.

His current research interests include high power converters and their control techniques in medium-voltage/high-voltage applications.